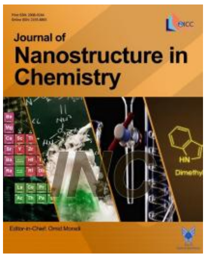
Journal of Nanostructure in Chemistry

J. Nanostruct Chem. 2026; 16(2): 112-127

Journal of Nanostructure in Chemistry (JNSC)

https://doi.org/10.57647/jnsc.2026.1602.06

Research Article

Electronic and Biocompatible Properties of Phosphorus-Doped 2D-Hexagonal Boron Nitride

Juliana Sales Osterno Leitão[1], Allysson Rocha Lima[1], Tiago Melo Freire[1], Felipe da Silva Barros[2], Antoninho Valentini[2], Juan Símon Rodriguez Hernández[3], Alejandro Pedro Ayala[3], Tayná Vitória Ramos de Oliveira[4,5], Ralph Santos-Oliveira[4,5], Alan Silva de Menezes[6], Beatriz da Silva Batista[7], Luciana Magalhães Rebêlo Alencar[7], Luelc de Souza Costa[8], Pierre Basílio Almeida Fechine[1],*

[1]*Advanced Materials Chemistry Group (GQMat), Department of Analytical Chemistry and Physical Chemistry, Federal University of Ceará – UFC, Campus do Pici, Fortaleza, CE ZIP Code, Brazil*
[2]*Department of Analytical Chemistry and Physical Chemistry, Federal University of Ceará, Campus of Pici, Fortaleza, Ceará, Brazil*
[3]*Department of Physics, Federal University of Ceará-UFC, Campus of Pici, Fortaleza, Ceará, Brazil*
[4]*Brazilian Nuclear Energy Commission, Nuclear Engineering Institute, Laboratory of Nanoradiopharmacy and Synthesis of New Radiopharmaceuticals, Rio de Janeiro, RJ, Brazil*
[5]*Rio de Janeiro State University, Laboratory of Nanoradiopharmaceuticals and Strategic Materials, Rio de Janeiro, RJ, Brazil*
[6]*Department of Physics, Federal University of Maranhão, Campus Bacanga, São Luís, MA, Brazil*
[7]*Department of Physics, Laboratory of Biophysics and Nanosystems, Federal University of Maranhão, Campus Bacanga, São Luís, MA, Brazil*
[8]*Brazilian Nanotechonology National Laboratory (LNNano), Brazilian Center for Research in Energy and Materials (CNPEM), Campinas, Sao Paulo, Brazil*

***Corresponding authors:** fechine@ufc.br

Article History:

Received:
10 July 2025

Revised:
10 October 2025

Accepted:
27 November 2025

Published in Issue:
30 April 2026

Abstract

Hexagonal boron nitride (h-BN) has been considered one of the most promising nanomaterials currently available, mainly due to its structural stability, high optical band gap, and promising biocompatibility. In this work, pure h-BN and phosphorus-doped derivatives (h-BN-1P and h-BN-1.5P) were synthesized by pyrolysis followed by heat treatment at 1000 °C under a nitrogen stream. Structural characterization was performed by PXRD, FTIR, and Raman spectroscopy, confirming the formation of the hexagonal phase and demonstrating that phosphorus incorporation did not disrupt the crystal lattice. AFM and SEM analyses identified a mixture of topographies, including 2D (nanosheets) and 1D (nanowhisker) morphological structures, and EDS confirmed the incorporation of phosphorus. TEM analysis allowed obtaining the determination of interplanar distance values for the samples. Cytocompatibility was assessed in human umbilical vein endothelial cells (HUVECs) through the MTT viability assay. The results indicated that pure h-BN maintained cell viability above 85%, while phosphorus-doped materials showed a slight decrease in viability, but still preserved viability levels above 50% at the maximum concentration evaluated (100 µg mL^{-1}). The results obtained confirm that h-BN and its phosphorus-doped forms exhibit favorable biocompatibility and tunable electronic properties, confirming their potential for future biomedical applications.

Keywords: Biocompatibility; Biomedical applications; Hexagonal boron nitride (h-BN); Phosphorous doping; Tunable electronic properties

---

Cite this article: Sales Osterno Leitão, J., Rocha Lima, A., Melo Freire, T., da Silva Barros, Antoninho Valentini, F., Símon Rodriguez Hernández, J., Pedro Ayala, A., Vitória Ramos de Oliveira, T., Santos-Oliveira, R., Silva de Menezes, A., da Silva Batista, B., Magalhães Rebêlo Alencar, L., de Souza Costa, L., Basílio Almeida Fechine, P., Electronic and Biocompatible Properties of Phosphorus-Doped 2D-Hexagonal Boron Nitride. *J Nanostruct Chem* **16**, 112-127 (2026). https://doi.org/10.57647/jnsc.2026.1602.06

Graphical Abstract

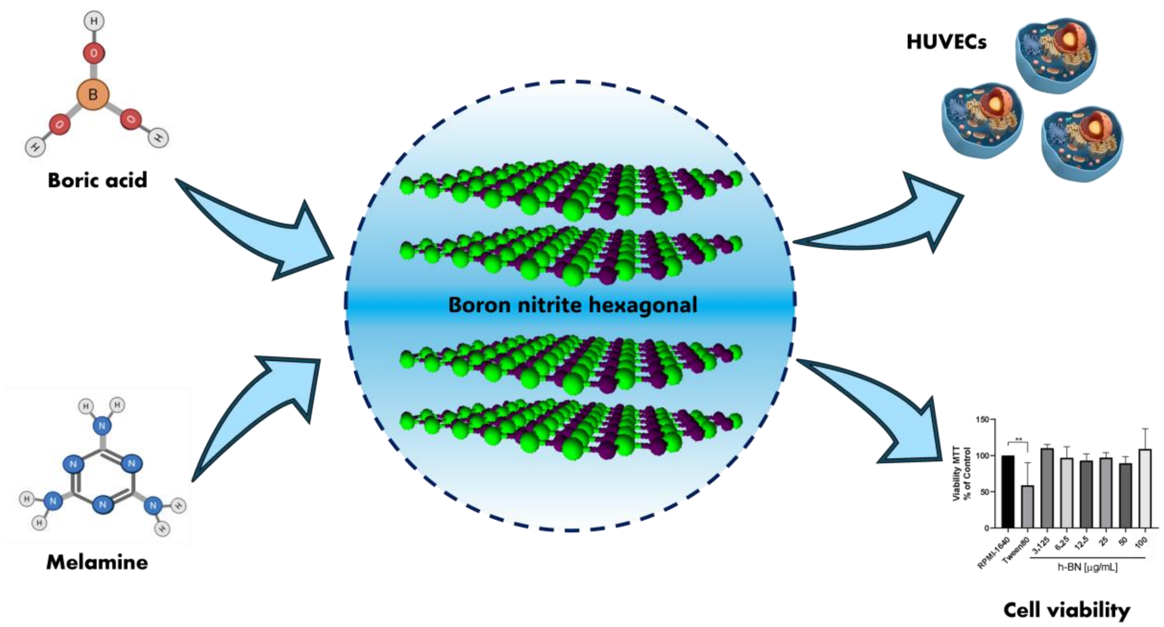

1. Introduction

Two-dimensional (2D) nanomaterials have enabled substantial advancements across a wide range of technological fields. These materials are characterized by their large lateral dimensions, high electrical conductivity, distinctive physicochemical properties, and unique structural features [1–3]. Beyond their appealing electronic, optical, and optoelectronic behaviors, the exceptional mechanical flexibility and robustness of 2D nanosheets have further expanded their applicability [4]. Graphene represents one of the most extensively studied examples, owing to its remarkable properties that support applications in biomedicine [5–7], energy storage [8–10], electronic devices [11], biosensors[12], among others. In recent years, hexagonal boron nitride (h-BN), another 2D material, has emerged as an important subject of study due to its remarkable intrinsic characteristics and range of possible applications.

The structure of h-BN consists of alternating boron and nitrogen atoms arranged in interlocking hexagonal rings, in which each B–N pair is connected through strong covalent bonds [13, 14]. Within individual layers, the B and N atoms are bonded through robust B–N covalent interactions, whereas adjacent layers are held together by weak van der Waals forces [15–17]. In contrast to graphene, where carbon atoms form purely covalent bonds, the B–N bonds in h-BN exhibit partial ionic character. This results from the stacking arrangement, in which boron atoms in one layer align vertically with nitrogen atoms in neighboring layers [13, 15, 16], leading to intrinsic bond polarity. As a result of these structural features, h-BN displays exceptional chemical and thermal stability and behaves as an electrical insulator with an optical bandgap of approximately 5–6 eV [18, 19]. Giving its favorable physicochemical properties, h-BN has found applications across multiple fields, including its use as an insulating material in electronic devices and as a component in anticorrosive coatings and high-temperature paints [20–24]. Moreover, h-BN has been extensively investigated for wastewater treatment and filtration due to its superior adsorption capacity and its suitability for membrane-based technologies [17, 25]. Its applicability has also been demonstrated in catalytic processes [23, 26], including the removal of emerging contaminants in water samples [27].

In addition, numerous studies have explored 2D nanomaterials, such as h-BN, for use in photovoltaic devices [28–30], optoelectronic [31, 32] and biosensing [33]. In recent years, the doping of h-BN with heteroatoms has emerged as a research area of significant interest. This strategy enables modulation of the h-BN bandgap and induces notable alterations in its electronic structure and surface chemistry [34, 35]. Among the various potential dopants, phosphorus has proven particularly promising due to its capacity to introduce new electronic states and modify the chemical reactivity of h-BN [36–39].

Consequently, phosphorus-doped h-BN exhibits enhanced optoelectronic and catalytic performance, prompting growing interest in understanding how these modifications influence the material's biological interactions. The use of 2D nanomaterials in biological applications requires careful study of their biocompatibility and cytotoxic effects [40, 41]. In this regard, pure h-BN has been studied extensively, mainly because of its chemical inertness and high biocompatibility, which has made it an excellent candidate for biomedical research [42–44].

However, the role of studying surface chemistry in modulating cellular responses remains critical, as the incorporation of doping agents can lead to distinct biological effects. In this context, this present work describes the synthesis and structural characterization of phosphorus-doped h-BN, and subsequently tested for cytocompatibility in human umbilical vein endothelial cells (HUVECs). By correlating structural modifications with cellular responses, this study provides new insights into the balance between functionalization strategies and biocompatibility, contributing to the advancement of h-BN–based nanomaterials aimed at future biomedical applications.

2. Methodology

2.1. Materials

Boric acid was purchased from Vetec with a purity of 99.5% (CAS number: 10043-35-3). Melamine was provided by Sigma-Aldrich with a purity of 99%, (CAS number: 108-78-1). Phosforic acid was purchased from Vetec with 85% purity (CAS number: 7664-38-2).

2.2. Synthesis of h-BN

h-BN was prepared by dissolving 9.28 g (0.15 mol) of boric acid together with 6.3 g (0.05 mol) of melamine in 500 mL of deionized water. After 10 minutes of stirring, the mixture was dried at 85 °C for 24 hours to remove the water. The dry precursor was then transferred to a quartz tube furnace and heated under flowing nitrogen at 1000 °C for 4 hours. Once the thermal treatment was completed, the obtained white solid was left to cool naturally to room temperature. It was then rinsed with deionized water and subjected to centrifugation to eliminate residual boric acid. The product was subsequently dried at room temperature (Figure 1).

2.3. Synthesis of phosphorous- doped h-BN

The h-BN-1P and h-BN-1.5P materials were prepared by dissolving boric acid (3.71 g, 0.06 mol), melamine (3.78 g, 0.03 mol), and phosphoric acid (1.0 g, 0.01 mol for 1P and 1.5 g, 0.015 mol for 1.5P) in 50 mL of deionized water. The mixtures were stirred for 10 minutes and subsequently dried at 85 °C.

The obtained precursor powders were then subjected to thermal treatment in a quartz tube furnace under a nitrogen atmosphere at 1000 °C for 4 hours. Once the material reached room temperature, the resulting solids were rinsed with deionized water, centrifuged to eliminate any remaining boric acid, and then allowed to dry at ambient conditions.

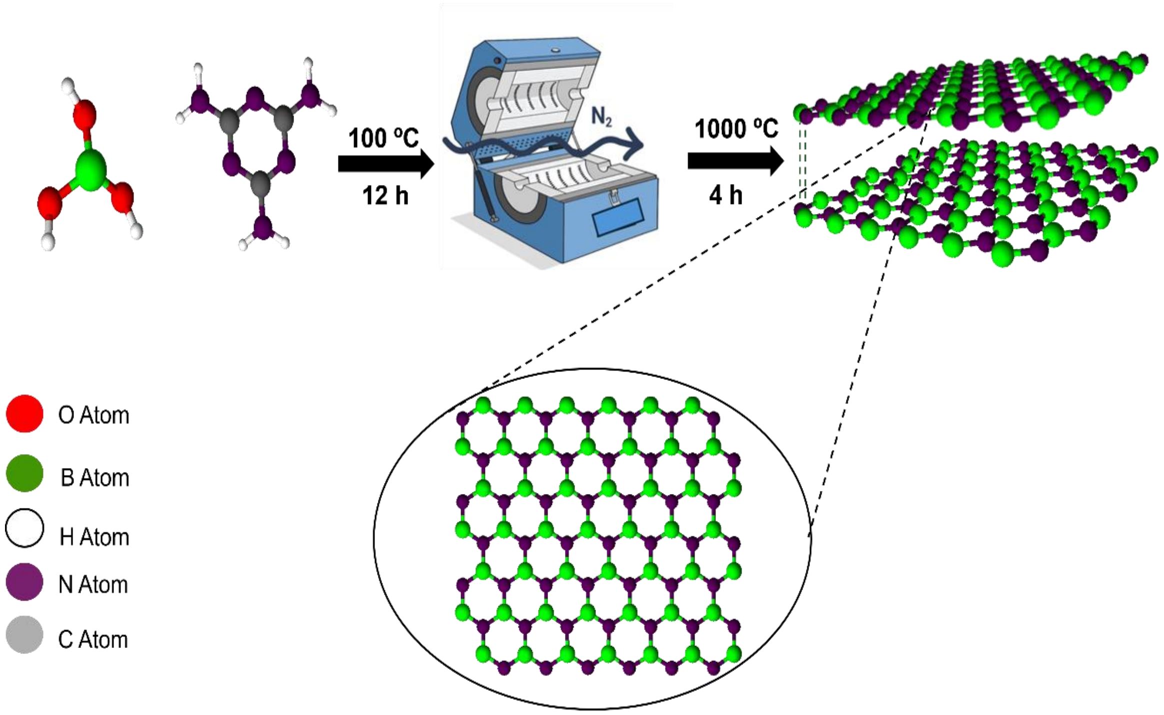

Figure 1. Schematic representation of the synthetic procedure used to obtain h-BN. The diagram illustrates precursor dissolution, drying, and high-temperature annealing under nitrogen, leading to the formation of layered h-BN with the characteristic hexagonal B–N arrangement

10.57647/jnsc.2026.1602.06

2.4. Characterization

The h-BN, h-BN-1P, and h-BN-1.5P samples were characterized by Powder X-ray diffraction (PXRD). The data were collected using a Bruker's X-ray diffractometer, model D8 Advance, operating with a Cu tube (λ = 1.54060 Å) and a LynxEye linear detector.

Measurements were carried out in the 2θ range of 10–90°, with a step size of 0.02° and a counting time of 0.4 s/step. Rietveld refinement was performed using the TOPAS V5 software. Fourier transform infrared (FTIR) spectra were obtain using a Shimadzu IRTracer-100 spectrophotometer.

Each sample was ground in an agate mortar and then compacted into KBr discs. Spectral analysis was performed over a range of 4000–400 cm^{-1}. The powder samples were analyzed by Raman spectroscopy using a high-resolution LabRam HR Horiba 800 system, featuring a grating of 1800 lines per millimeter and a Syncerity detector. Excitation was provided by the 632.5 nm emission of a He–Ne laser, and the light was directed onto the sample using a 100/0.90 long-working-distance objective.

Measurements were obtained using a spectrophotometer (Shimadzu, UV-2600), and the band gap was derived by applying the Kubelka–Munk transformation to the reflectance data. Surface topography and potential data were measured using Kelvin Probe Force Microscopy (KPFM). For AFM analysis, the materials were deposited on mica and imaged with a Bruker Multimode 8 system equipped with a Nanoscope 2.1 controller. The measurement was performed using a Si probe (Bruker, PFQNE-AL) with a spring constant of 0.4 N/m, lift height of 70 nm, maps with a resolution of 256 x 256 pixels, with a scanning frequency set to 1 kHz.

During the measurements, the laboratory conditions were approximately 25 °C and 44% relative humidity. Data processing was performed using Nanoscope 2.0 and Gwyddion software.

Scanning Electron Microscopy (SEM) images were obtained using a Zeiss microscope, model EVO 15, with a high-vacuum SE detector. Energy Dispersive Spectroscopy (EDS) data were acquired with an XFlash 410 detector from Bruker.

The samples were coated with Au to make their surfaces conductive. Transmission electron microscopy (TEM) analyses were carried out on a Thermo Fisher/FEI F200 instrument operating at 200 kV and fitted with a 4k × 4k Ceta CMOS camara. Imaging was conducted using a parallel beam under conventional TEM (CTEM) conditions.

For sample preparation, a 3 µL drop of the sonicated suspension was placed onto a 400-mesh copper grid covered with an ultrathin carbon layer, and the grid was left to dry at ambient temperature.

2.5. Cell Viability

HUVECs were used to perform the cell viability assays. Cells were initially expanded in T75 cm^2 culture flasks and maintained in an incubator at 37 °C, with 5% CO_2 and 95% humidity. Upon reaching the appropriate confluence, cells were seeded into 96-well plates at a density of 1×10^4 cells per well. Cell adhesion was assessed 24 hours after seeding, at which point treatments were applied at concentrations of 3.125, 6.25, 12.5, 25, 50 and 100 µg mL^{-1}. After 24 hours of incubation, MTT solution (1 mg mL^{-1}) was added and allowed to react with the cells for 3 hours to enable formazan formation. The resulting crystals were dissolved in DMSO, and absorbance was recorded at 450 nm using a microplate reader. Absorbance values were expressed as a percentage relative to the untreated control, set as 100%. All assays were performed in quadruplicate. Data analysis was carried out using GraphPad Prism 8.0, applying one-way ANOVA followed by Dunnett's post hoc test. Results are presented as mean ± standard error of the mean (SEM), and differences were considered statistically significant at $^*p < 0.05$.

3. Results and discussion

3.1. Structural and chemical characterization

The PXRD patterns and Rietveld refinement obtained for the h-BN, h-BN-1P, and h-BN-1.5P samples are shown in Figure 2a. Initially analyzing the h-BN diffractogram, it is possible to observe the presence of four characteristic peaks located at approximately 26.1°, 42.4°, 61.6°, and 76.1° that were assigned to (002), (100), (004), and (110) planes, respectively [45, 46], belong to the P63/mmc hexagonal space group (ICSD 241875). In the diffractogram of the h-BN-1P sample, it is also possible to observe the presence of the hexagonal BN phase peaks. However, the (002) peak presents a distorted shape, indicating the presence of two hexagonal BN phases with different lattice parameters and microstrain/crystallite size distributions. These two hexagonal BN phases were introduced in the Rietveld refinement, and their lattice parameters, microstrains (ε), crystallite sizes (D), and phase concentrations are shown in Table 1. As can be seen in Table 1, one BN phase has a smaller crystallite size (BN-s) and the other one has a larger crystallite size (BN-l). The h-BN-1P sample also presents three other phases: the ammonium borate hydrate ($NH_4B_5O_8 \cdot 4H_2O$, ICSD: 90001), boron phosphate (BPO_4, ICSD: 26890), and phosphorus oxide (P_2O_5, ICSD: 29045). For h-BN-1.5P, the formation of a second phase is also observed, corresponding to the formation of the BPO_4 species. The presence of this species led to an increase in the width of the (002) peak. Such an observation may indicate a decrease in the average size of the crystallites [47].

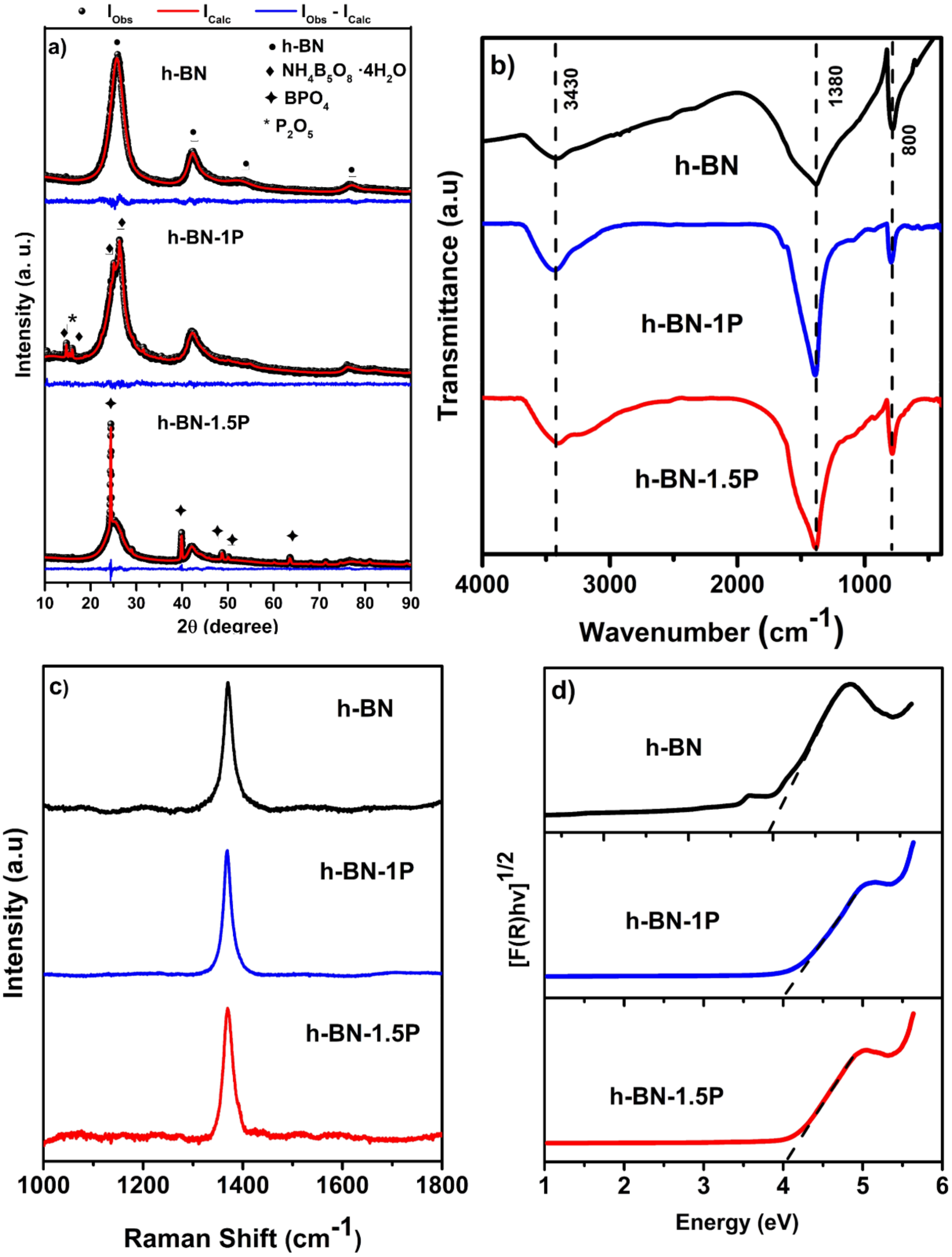

Figure 2. a) PXRD patterns of h-BN, h-BN-1P, and h-BN-1.5P, showing the crystallographic features associated with the hexagonal BN phase and the changes introduced by phosphorus incorporation; b) FTIR spectra of the three samples, displaying the fundamental vibrational modes of B–N bonds and additional bands originating from phosphorus-related functional groups; c) Raman spectra highlighting the characteristic phonon mode of hexagonal BN and the spectral modifications observed upon phosphorus addition; d) Tauc plots constructed from diffuse-reflectance UV–Vis data, used to estimate the optical band gaps of the materials

The formation of BPO_4 in the h-BN-1.5P sample occurred due to the proportion of boric acid and phosphoric acid precursors. These two precursors react to the formation of BPO_4, however, depending on the temperature to which the reaction is submitted, the phosphate can be soluble or insoluble in water. The reaction in this study occurred at 1000°C, leading to the formation of phosphate insoluble in water, making it impossible to remove the contaminant after washing. However, after Rietveld refinement, it was possible to determine that the BPO_4 phase corresponded to only 5.3% of the sample, and then the remainder (94.7%) was composed of phosphorus-doped h-BN, as of interest [48]. Figure 2b presents the FTIR spectra obtained after the analysis.

For the h-BN spectrum, it is possible to observe the presence of band at 800 cm^{-1} is attributed to the out-of-plane bending of the B-N-B bond.

10.57647/jnsc.2026.1602.06

Table 1. Structural parameters obtained from Rietveld refinement of the PXRD data for h-BN, h-BN-1P, and h-BN-1.5P, including the refined lattice constants, crystallite size, microstrain, and the relative fraction of each identified phase

Sample	Phase	a (Å)	c (Å)	D (nm)	ε (%)	Rwp (%)	S	Concentration (%)
h-BN	BN	2.482 (1)	6.982 (9)	3.7 (1)	0.43 (4)	3.9	1.3	100.0
h-BN-1P	BN-s	2.469 (1)	6.969 (5)	4.1 (3)	0.58 (6)	3.6	1.2	95.4 (3)
	BN-1	2.502 (1)	6.696 (3)	8.4 (7)	0.19 (5)			2.5 (4)
	$NH_4B_5O_8 \cdot 4H_2O$	-	-	-	-			1.5 (9)
	BPO_4	-	-	-	-			0.3 (1)
	P_2O_5	-	-	-	-			0.3 (1)
h-BN-1.5P	BN	2.479 (5)	7.057 (2)	8.1 (6)	0.60 (3)	4.6	1.3	94.7 (2)
	BPO_4	-	-	-	-			5.3 (2)

The existence of a B-N bond was identified by the presence of a band at 1380 cm^{-1} [49, 50] bond is also observed. In the region between 3100 and 3450 cm^{-1}, there is the presence of a broadband attributed to the presence of O-H bonds and amino groups in the structure of the nanomaterial [51]. Analyzing the spectra obtained for the h-BN-1P and h-BN-1.5P samples, it is possible to observe that the main bands did not suffer displacement, indicating that the structure of the hexagonal boron nitride was maintained. In addition, there was the emergence of small, less intense bands in the range of 850 to 1200 cm^{-1}, indicating the existence of B−O and B−O−H bonds [48, 52]. When analyzing hexagonal boron nitride by Raman spectroscopy, it is common to observe the presence of a dominant band around 1365-1370 cm^{-1}. The Raman spectrum obtained for the h-BN, h-BN-1P and h-BN-1.5P samples (Figure 2c) has a single band located at 1368 cm^{-1}, assigned to the E_2g vibration mode [53–55]. It corresponds to the vibration in the plane of the boron and nitrogen atoms in the hexagonal lattice, being analogous to the G-mode of graphene, but with displacement because of the difference in atomic mass and strength of the B-N bonds. The presence of this single band is also an indication that boron nitride is in hexagonal form, since, depending on the form of arrangement, the band may appear in another region [56]. The DRS technique was employed for the analysis of the optical properties of the samples and is shown in Figure 2d. It is possible to observe that all samples presented absorption bands in the UV region, being located at 255 nm for h-BN, 244 nm for h-BN-1P, and 247 nm for h-BN-1.5P. Using the Kubelka-Munk model, the three samples were analyzed, and the obtained F(R) values were plotted using Tauc coordinates for allowed direct transitions. In this way, it was possible to evaluate the energy gap width of all samples. Using the linearization technique, an energy gap width value Eg of 3.87 eV for h-BN was obtained from the linearized section analysis in the optical absorption edge range (see Figure 2d). Several studies report that hexagonal boron nitride exhibits an optical bandgap of approximately 5.87 eV [57–62]. However, it is well established that this value can vary widely depending on the synthesis route, as well as on factors such as impurities, the incorporation of dopants, and other structural or chemical modifications [58, 59, 61, 62]. Zhu et al. [63]for instance, reported an optical bandgap of 3.8 eV for h-BN with a nanowhisker morphology, a result consistent with those obtained in our study. Comparable observations have also been described by Rand and Roberts [64], who obtained boron nitride thin films exhibiting a bandgap of 3.8 eV, and by Ba et al. [65], who synthesized h-BN samples with a notably lower optical bandgap of 2.11 eV. The h-BN-1P and h-BN-1.5P samples exhibited optical band gap values of 4.04 eV and 4.06 eV, respectively. While these values are significantly lower than typically reported for bulk hexagonal boron nitride (approximately 5.9 eV), characterizing them as the defect-mediated optical band gap of the nano-structured material, a key observation is that the doped samples show a distinct increase in band gap relative to the h-BN reference sample (3.87 eV). This increase is primarily attributed to the structural strain generated by phosphorus incorporation. Specifically, because phosphorus has a larger atomic radius than the nitrogen it replaces, its substitution forces the expansion of the interplanar distance d_{002} (from 0.347 nm to 0.367 nm). In two-dimensional materials, increasing the interlayer spacing reduces the electronic coupling between the planes, which in turn elevates the band gap energy [66], demonstrating successful band gap tuning via structural deformation. Furthermore, the electronic modulation is solely attributed to the phosphorus incorporation into the h-BN network and not to secondary phases. The trace amounts of P_2O_5 detected (at 0.3%) are negligible, and the BPO_4 phase (at up to 5.3%) possesses a very high intrinsic band gap of approximately 7.3 eV [67]. Since this value is considerably larger than the measured band gap of the doped samples (~ 4.0 eV), the minority presence of BPO_4 does not interfere with the absorption edge used to determine the optical band gap via the Tauc method. Therefore, the observed band gap modulation is confirmed because of the doping effect. This finding aligns with studies showing that other n-type dopants can induce similar band gap modulation effects when introduced into h-BN [59, 68].

3.2. Surface and morphological properties

To further studies on the morphology of h-BN, the atomic force microscopy (AFM) technique was used. To enable high-resolution imaging, the sample was deposited on a freshly cleaved mica substrate, which provides an atomically smooth surface. The region with h-BN is thicker (~ 1.7 nm), while the mica is about 0 nm(base) (Figure 3a). The morphology is flat with well-defined edges, typical of exfoliated 2D materials. The h-BN region presents a higher surface potential (~ 0.21 V) compared to the mica (~ -0.1 V), and this potential difference is associated with the difference in the work function between h-BN and mica. The height contrast reveals a relatively flat flake with a maximum height of approximately 1.7 nm (line profile). Considering that the thickness of a monolayer of h-BN ranges from approximately 0.3 [69, 70], the analyzed sample contains approximately 5 layers. The potential mapping shows a clear contrast between the NB flake and the mica. Mica has a lower surface potential, while h-BN has a higher potential. The potential difference observed in the profile is approximately 0.13 V. This variation indicates changes in the local work function, which are associated with the surface's electron density. Analyzing the work function graph, the presence of two peaks fitted by Gaussian deconvolution is observed. The first peak is located at 4.21 eV and the second peak at 4.23 eV. The work function values for h-BN found in this work agree with values found in other studies [71, 72]. Analyzing the other height image (Figure 3b), the presence of h-BN flakes with different heights was observed.

The height of the flakes was indicated in the profiles, with the thinnest flake having a height of approximately 1.37 nm and the thickest flake having a height of approximately 5.88 nm. As previously stated, the thickness of a monolayer of h-BN varies from approximately 0.3[69, 70], so that the thickness of these flakes corresponds to approximately 4 layers and 19 layers, respectively. Analyzing the work function graph, the presence of two peaks adjusted by Gaussian deconvolution is also observed.

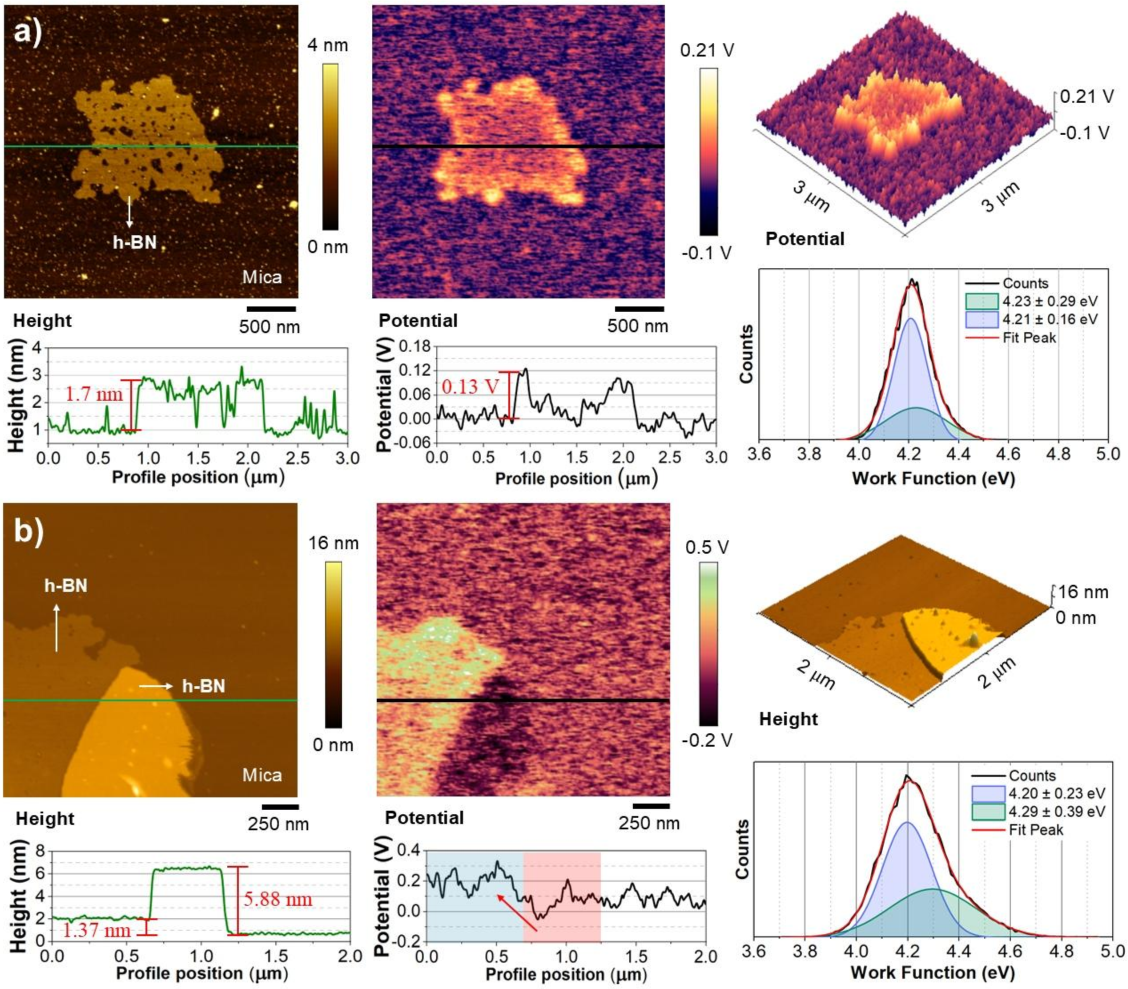

Figure 3. a) Topographic (Height) and surface potential maps of an h-BN flake. The line profiles show the height (~1.7 nm, corresponding to approximately 5 layers) and the potential difference (~0.13 V) between the h-BN flake and the mica substrate. The graph on the right shows the work function with two Gaussian peaks at 4.21 eV and 4.23 eV; b) Topographic (Height) and surface potential maps of h-BN flakes with varying thicknesses. The height profiles reveal a thinner flake of approximately 1.37 nm (~4 layers) and a thicker flake of approximately 5.88 nm (~19 layers). The work function graph displays two Gaussian peaks at 4.20 eV and 4.29 eV

10.57647/jnsc.2026.1602.06

The first peak is located at 4.20 eV and the second peak at 4.29 eV, and these values are also in agreement with other studies already reported [73, 74].The surface potential distribution (Figure 3b) shows that increasing the thickness of h-BN films reduces their work function. This trend indicates that samples with fewer layers require more energy to extract an electron, a dependence also observed in other two-dimensional materials [75, 76]. However, it was not possible to obtain AFM/KPFM data for the h-BN-1P and h-BN-1.5P samples, even after modifications to the substrate surface, because the adhesion force between the probe and the material became greater than the force that held the sample to the substrate during scanning. It is suggested that changes in structural and electronic properties induced by P doping intensified the probe-sample interaction. XRD results (Figure 2a) confirm the presence of different crystalline phases in the doped samples, indicating a structural modification. In parallel, an electronic modification is observed in the DRS results (Figure 2d), with an increase of ~0.18 eV in the band gap in the doped samples. Therefore, the inability to attach the doped samples to the substrate is also evidence of the modification of surface properties after doping. The SEM technique was employed in order to obtain information about the morphology of the samples (Figures 4a, 4c and 4e). It can be observed that the samples present a mixture of two-dimensional structures in the form of sheets and whiskers[77, 78]. The presence of a mixture of 2D and 1D morphologies can bring benefits, as the presence of nanowhiskers can act as an interconnector for 2D nanosheets, preventing their stacking and preserving the high surface area and accessibility of 2D morphology. Niu and collaborators [79] presented a similar study, in which they used alumina spheres (3D) joined to h-BN nanoflakes (2D) and evaluated the effects of mixing morphologies.

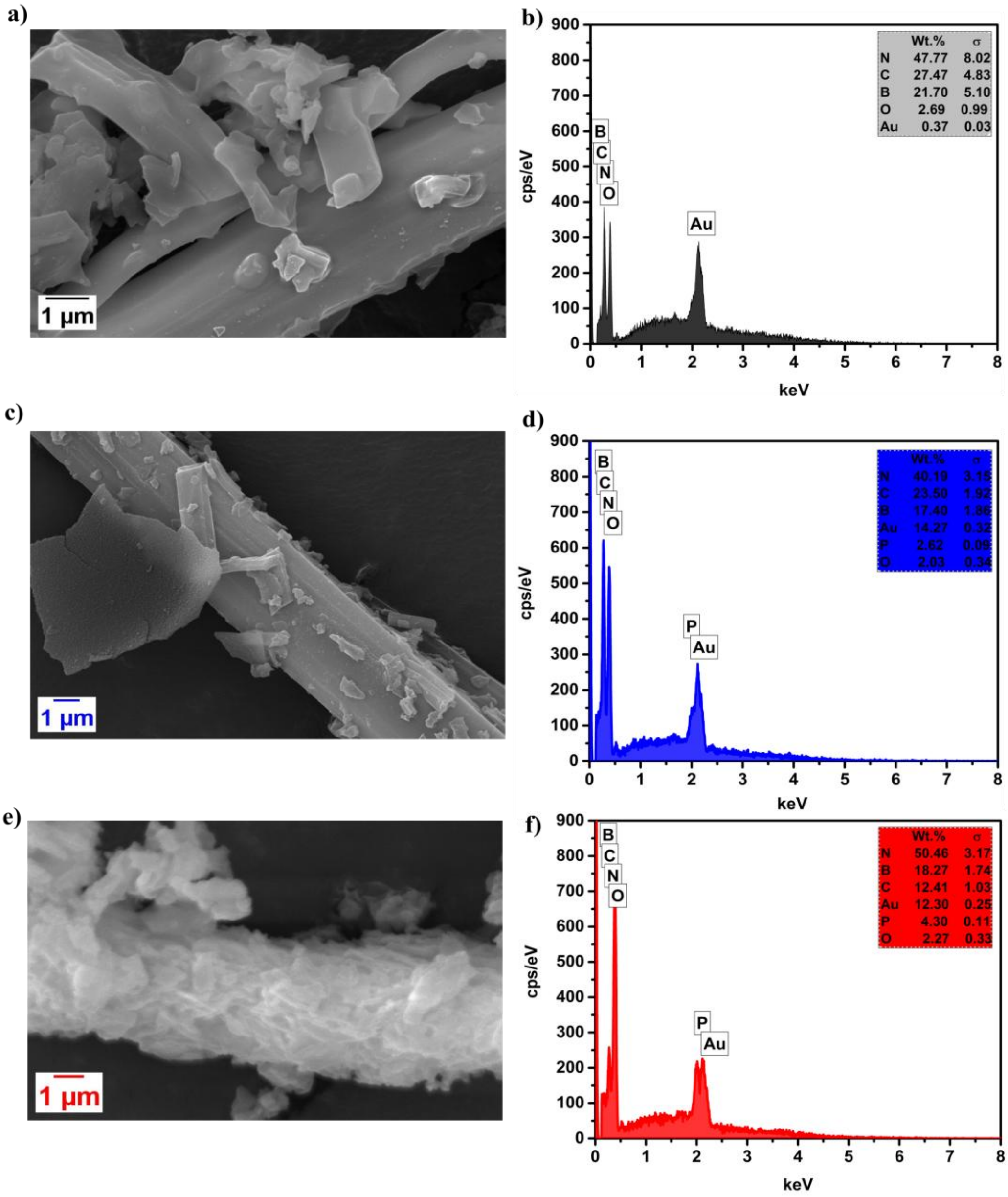

Figure 4. a), c), e) SEM images of h-BN, h-BN-1P, and h-BN-1.5P, showing the morphology and surface features of each sample. b), d), f) EDS spectra and elemental distribution maps corresponding to the samples, illustrating the spatial distribution of boron, nitrogen, and phosphorus

10.57647/jnsc.2026.1602.06

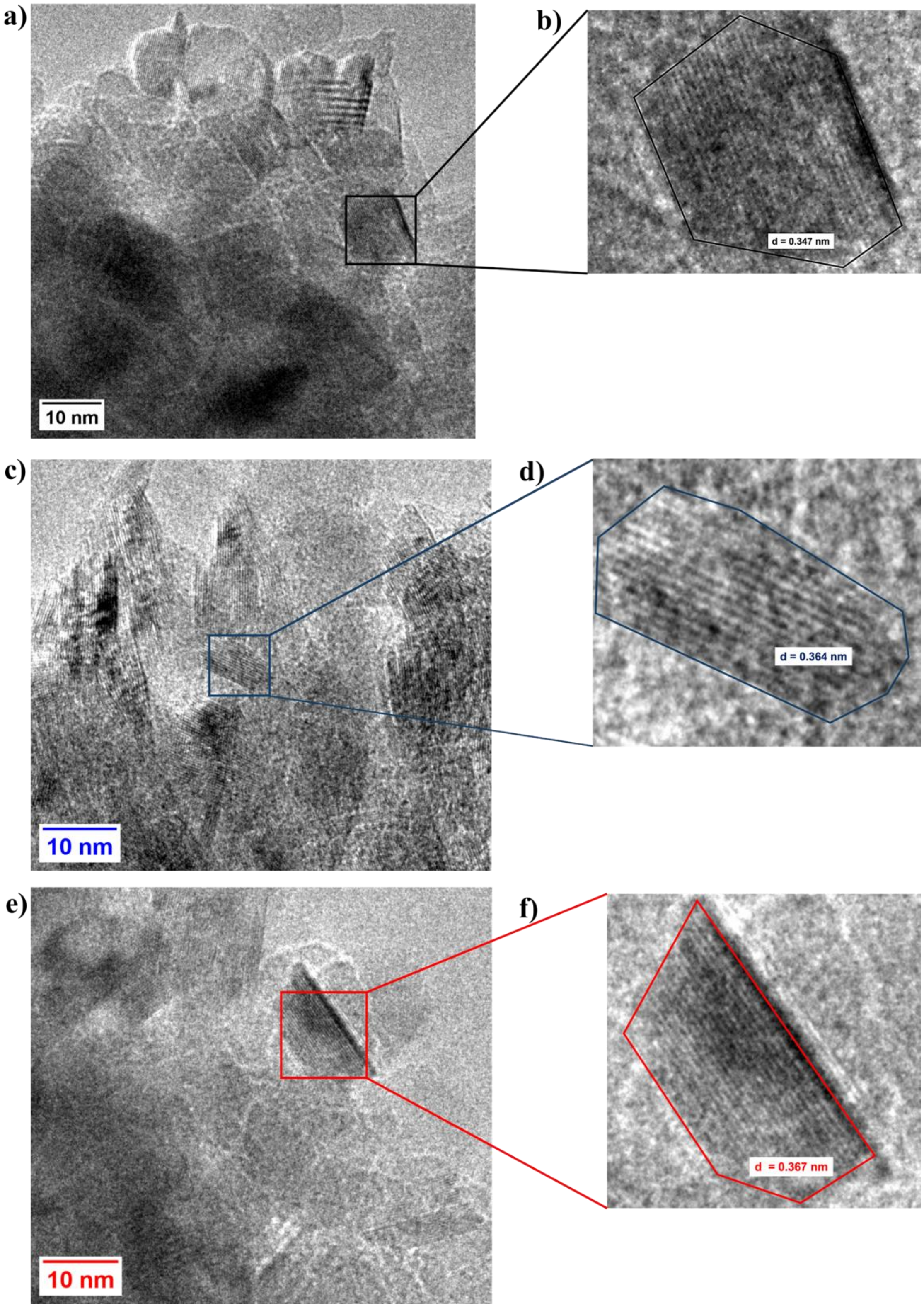

Figure 5. a), c), e) TEM images of the h-BN, h-BN-1P, and h-BN-1.5P samples, showing the nanosheet structures and morphological characteristics. b), d), f) High-resolution TEM (HRTEM) images highlighting the layered architecture of the materials and the lattice fringes associated with the BN planes

The element distribution map in Figure S1 clearly shows an adequate distribution of boron and nitrogen elements on the surface of h-BN. The element distribution map of samples h-BN-1P, and h-BN-1.5P (Figure S2 and S3) also shows the distribution of boron, nitrogen, and phosphorus on the surface of the samples. The EDS analysis of sample h-BN (Figure 4b) shows the presence of both boron and nitrogen. For samples h-BN-1P and h-BN-1.5P, the spectrum obtained by EDS analysis (Figures 4d and 4f) confirms the existence of boron, nitrogen, and phosphorus atoms in the samples. A comparative analysis of the mass ratios of boron, nitrogen, and phosphorus in each sample was performed. The N/P ratios of the h-BN-1P and h-BN-1.5P samples were 15.33 and 11.73, respectively, while the N/B ratios for the same samples were 6.64 and 4.24. Analyzing the values obtained, a decrease is observed. This was expected, since phosphorus, when added to the structure, occupies spaces previously filled by nitrogen atoms. The samples were submitted to TEM analysis, through which images were obtained showing the structure in the shape of sheets (Figure 5). The interplanar distance (*d*) was calculated for all samples. The h-BN sample presented a *d* value equal to 0.347 nm, and this value is higher than the interplanar distance normally reported for h-BN with high crystallinity (0.333 to 0.334 nm) [80]. This disparity in the value can be attributed to the occurrence of disordered stacking between the layers, called turbostratic stacking [81]. This type of stacking presents itself as an intermediate between crystalline h-BN and h-BN in the amorphous phase [82]. In addition, it weakens the van der Waals interaction of the layers [83], which leads to an expansion of the crystal lattice in the direction perpendicular to the planes (c axis), directly resulting in an increase in the d_{002} distance to 0.347 nm. However, studies by Kumar et al. analyzed the morphology of h-BN crystals and reported interplanar distances of 0.34 nm for nanowhiskers and 0.36 nm for nanosheets [84]. Figure S4 shows a lower-magnification microscopy of the h-BN sample, in which two types of structures can be observed. The image shows broad, flat, non-contrasting, translucent regions, typical of h-BN nanosheets, and elongated, more contrast-rich, fibrillar structures that project from the edges of the sheets or are partially isolated. These thinner, linear structures resemble nanowhiskers, as they exhibit anisotropic stretching, with length much greater than thickness and width. The phosphorus-doped samples showed interplanar distance values of 0.364 nm and 0.367 nm for h-BN-1P and h-BN-1.5P, respectively. The increase in the values of interplanar distance in the phosphorus-doped samples when compared to the d-value of the h-BN sample evidence the incorporation of phosphorus into the network. The phosphorus atom has a larger atomic radius than the nitrogen it replaces, inducing a high degree of voltage in the lattice. This stress is relieved by increasing the distance between the layers, resulting in an expansion of the crystal lattice along the c-axis, but the values found agree with the values found by Kumar and collaborators for h-BN nanosheets [84]. Figures S5 and S6 show low-magnification transmission electron microscopy images of the h-BN-1P and h-BN-1.5P samples, respectively. Both images demonstrate the presence of lamellar structures with well-defined edges, typical of h-BN nanosheets.

3.3. Cell viability

The cytotoxicity of phosphorus-doped hexagonal boron nitride (h-BN-1P) and highly doped h-BN (h-BN-1.5P) was assessed using the MTT assay in human umbilical vein endothelial cells (HUVECs) following 24 h exposure to increasing concentrations (3.125–100 µg mL^{-1}) (Figure 6). Pristine h-BN exhibited the highest biocompatibility, with cell viability consistently exceeding 85% across all tested concentrations, corroborating its well-documented chemical inertness and low biointeractivity [85, 86].

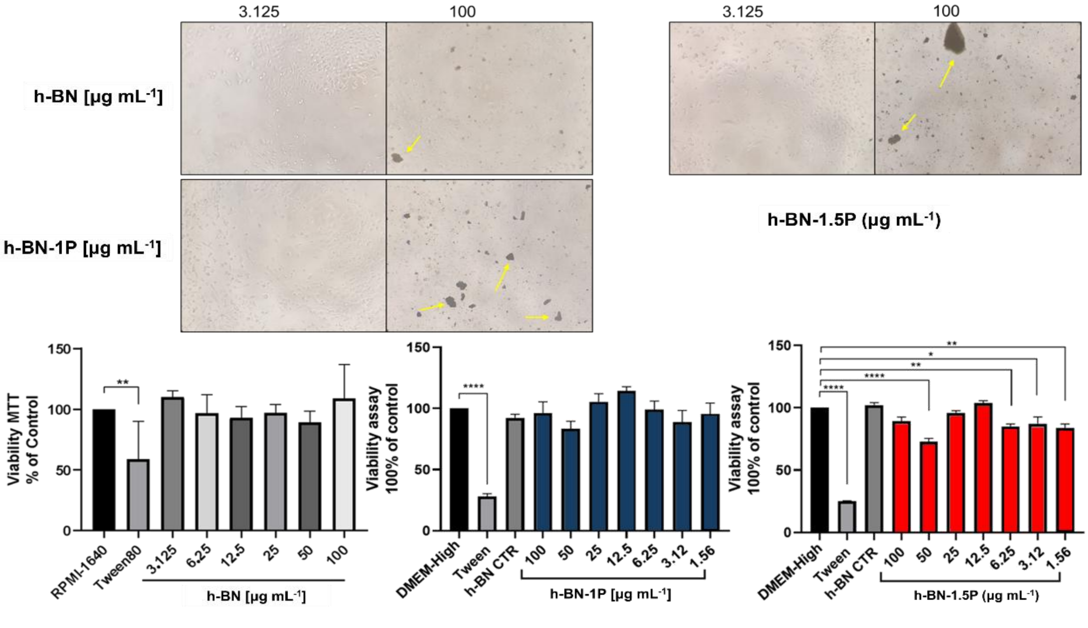

Figure 6. Optical microscopy images of HUVECs after 24 h exposure to pristine h-BN, phosphorus-doped h-BN (h-BN-1P), and highly doped h-BN (h-BN-1.5P). Yellow arrows indicate the presence of h-BN aggregates. Cell viability was assessed by MTT assay at increasing concentrations (1.56–100 µg mL^{-1}). Pristine h-BN showed minimal impact on viability, while phosphorus doping led to a dose-dependent decrease, more pronounced with h-BN-1.5P. Results are expressed as mean ± SEM, normalized to untreated control (100%)

Table 2. Numerical representation of the mean and SEM values for the cell viability assay (MTT). The data show the controls (medium, Tween, and h-BN) and the concentrations of each compound when phosphate is presence (h-BN 1P and h-BN 1.5P)

Conditions	h-BN 1.0P	h-BN 1.5P
Medium	100 ± 0.0	100 ± 0.0
Tween 10% (v/v)	28.0 ± 2.2	25.2 ± 0.2
h-BN	92.2 ± 3.0	102.1 ± 2.0
100 [μg mL^{-1}]	96.2 ± 9.2	89.2 ± 3.3
50 [μg mL^{-1}]	83.4 ± 6.2	72.8 ± 2.6
25 [μg mL^{-1}]	105.5 ± 6.5	95.9 ± 1.7
12.5 [μg mL^{-1}]	114.5 ± 3.3	104 ± 1.6
6.25 [μg mL^{-1}]	99.2 ± 6.8	85.1 ± 1.9
3.125 [μg mL^{-1}]	88.7 ±9.6	87.2 ± 5.5
1.56 [μg mL^{-1}]	95.3 ± 9.0	84.0 ± 3.0

The introduction of phosphorus resulted in a concentration-dependent decline in viability. h-BN-1P induced moderate cytotoxicity, maintaining cell survival above 83% up to 50 μg mL^{-1} (not significant). In contrast, h-BN-1.5P elicited a more substantial reduction in viability, decreasing to approximately 72.8 ± 2.6% at 50 μg mL^{-1}. Table 2 shows the mean values ± standard deviation of the mean, corroborating the data plotted in the graph.

These findings indicate that although pure h-BN exhibits high cytocompatibility, phosphorus doping alters its interaction with biological systems. This effect is likely associated with modifications in surface chemistry and electronic structure, as supported by structural characterization data. In particular, the emergence of B–O and B–O–H vibrational modes in FTIR spectra and the presence of BPO_4 secondary phases identified by PXRD suggests the formation of more reactive surface sites in doped samples [87–90].

An important result observed in this study is that all samples-maintained cell viability above 50%, although they exhibited cytotoxic effects at higher concentrations, a threshold commonly considered acceptable in preliminary nanotoxicological assessments. These results indicate that phosphorus doping introduces a functional trade-off: while it may enhance desirable properties such as bandgap modulation and increased surface polarity, it also leads to a moderate reduction in cytocompatibility [47, 91]. Such a balance between improved material functionality and biological safety must be carefully evaluated when considering potential biomedical applications, particularly in contexts involving prolonged exposure or systemic administration.

When compared with other doped two-dimensional (2D) materials, phosphorus-doped h-BN exhibits a notably favorable cytocompatibility profile. While pristine h-BN consistently supports high cell viability (> 85%) due to its chemical inertness, phosphorus doping (h-BN-1P and h-BN-1.5P) induces only a modest decline in cell survival, maintaining viability remaining above 50% even at 100 μg mL^{-1}. This behavior contrast with doped graphene analogs, such as nitrogen- or boron-doped graphene, which often exhibit dose-dependent cytotoxicity associated with oxidative stress and membrane perturbation, particularly at concentrations exceeding 50 μg mL^{-1} [5, 7]. Likewise, transition metal-doped MoS_2 systems have been reported to induce elevated reactive oxygen species (ROS) generation and mitochondrial disruption in similar *in vitro* models [92]. Overall, phosphorus-doped h-BN materials offer an advantageous biocompatibility-to-functionality ratio, reinforcing their potential use in biomedical fields, including drug delivery, biosensing, and bioelectronic devices. The combined 2D-1D morphology further benefits cellular interactions, particularly for HUVECs, by providing expanded contact surfaces through nanosheets while nanowhisker segments act as additional anchoring points that promote adhesion and spreading [93]. Furthermore, the tunable bandgap and acceptable cytocompatibility underscore their promise as alternatives to more cytoreactive 2D systems. Nonetheless, comprehensive in vivo studies and mechanistic investigations will be essential to fully establish their safety margins and immunological profiles.

It is important to note that although the acute cytocompatibility of h-BN and its phosphorus-doped derivatives was favorable, the long-term stability of these materials under physiological environments remains to be fully characterized. Pure h-BN is known for its robust chemical inertness, however, the introduction of phosphorus results in the formation of B–O and P–O moieties, which may be susceptible to hydrolysis or oxidative degradation over time. Such processes could lead to gradual release of borate or phosphate species and induce dynamic surface restructuring, potentially altering biocompatibility in prolonged exposures. Accordingly, future investigations will focus on long-term incubation studies in simulated body fluids and serum-supplemented media, detailed analysis of degradation product, and evaluation of chronic cellular responses, thereby establishing the in vivo relevance and long-term biosafety of these materials.

The electronic modulation introduced by phosphorus [94] doping in h-BN position these materials as promising candidates for targeted biomedical applications. This effect is evidenced by the shift in optical bandgap values to 4.04 eV and 4.06 eV for h-BN-1P and h-BN-1.5P, respectively, compared with 3.87 eV for pure h-BN. First, in drug delivery, the increased surface reactivity from dopant-induced B–O and B–O–H functional groups may facilitate drug conjugation or enable pH-responsive release mechanisms, while the preserved 2D morphology provides a high surface-area loading. Second, the bandgap modulation achieved through phosphorus doping supports potential applications in biosensing, as the associated enhancements in charge transport and surface polarity are critical for the development of electrochemical and photonic sensors with improved sensitivity [95–99]. Additionally, the partial electronic conductivity introduced by phosphorus atoms may enable integration into bioelectronic platforms, allowing h-BN–P materials to function as dielectric substrates or semiconducting layers in flexible or implantable devices. Although less extensively studied, their chemical stability and moderate cytocompatibility also suggest suitability for incorporation into tissue-engineering scaffolds, particularly for electrically responsive tissues such as neural or cardiac systems, where localized electronic cues can modulate cell behavior. Together, these functionalities underscore the dual role of phosphorus doping: conferring tunable optoelectronic properties while maintaining cytocompatibility levels acceptable for early-stage biomedical evaluation.

Beyond their biocompatibility and structural integrity, the phosphorus-induced tuning of the electronic band structure in h-BN-P materials introduces functional capabilities that may be exploited in electroactive and photoresponsive biomedical systems [93, 100, 101]. The observed bandgap narrowing (to ~4.04 – 4.06 eV) suggests improved charge-carrier behavior, potentially enabling applications such as photothermal therapy, photoelectrochemical biosensing, or electrically stimulated tissue regeneration. These electronic transitions, combined with the presence of B–O and B–O–H moieties, suggest enhanced interfacial charge dynamics critical for bioelectronic device performance. Although not directly explored in this study, future investigations will focus on assessing photoconductivity and electrochemical response in aqueous and physiological conditions to validate their suitability for such applications.

4. Conclusion and future perspectives

This study proposes the synthesis h-BN nanomaterial by pyrolysis followed by heat treatment at 1000 °C under nitrogen flow, as well as the production of its phosphorus-doped variants by the same synthetic route. FTIR analysis revealed the characteristic bands of h-BN, in agreement with the literature, demonstrating that phosphorus doping did not significantly alter the material's crystal structure. Raman spectroscopy revealed the typical band associated with the E_{2g} vibrational mode, confirming the formation of the hexagonal phase. The PXRD diffractograms corroborated the structural results, allowing us to evaluate the effects of doping and demonstrating the preservation of the hexagonal lattice even after the incorporation of phosphorus.

The optical bandgap calculation indicated the production of h-BN with a reduced value (3.87 eV) compared to that reported in the literature (~ 5.8 eV). Furthermore, doping further reduced the optical band gap, reaching values of 4.04 eV and 4.06 eV for h-BN-1P and h-BN-1.5P, respectively, highlighting the effect of the structural modification on the material's electronic properties.

AFM images revealed a typical topography of exfoliated 2D materials, with defined edges and an average height of approximately 1.7 nm. Work function measurements were consistent with previously reported data. SEM micrographs revealed two distinct morphologies—nanosheets (2D) and nanowhiskers (1D)—for h-BN and its doped samples. Through EDS analysis, it was possible to obtain relevant knowledge about the chemical composition, mainly confirming the presence of phosphorus in the doped materials.

Assessment of cell viability in human endothelial cells (HUVECs) demonstrated that h-BN exhibited high cytocompatibility at all concentrations tested, with values above 85% compared to the control. Phosphorus doping resulted in a slight reduction in viability, especially at higher concentrations, although all samples-maintained survival rates above 50%, a parameter generally considered acceptable in preliminary studies of nanomaterials. Overall, the results obtained confirm that h-BN and its phosphorus-doped forms exhibit promising biocompatibility, with pure h-BN being the safest formulation for endothelial cells. These findings reinforce the material's potential for biomedical applications, although additional studies involving prolonged exposure, mechanistic studies of cellular interaction, and evaluation in tumor-relevant models are essential to further explore their therapeutic potential and safety boundaries.

Credit authorship contribution statement
Juliana Sales Osterno Leitão: Writing – original draft; Writing – review & editing; Methodology; Investigation; Formal analysis; Data curation. Allysson Rocha Lima: Methodology; Investigation; Formal analysis. Tiago Melo Freire: Writing – original draft; Methodology; Investigation; Formal analysis. Felipe da Silva Barros: Methodology; Investigation. Antoninho Valentini: Methodology; Investigation; Formal analysis. Juan Símon Rodriguez Hernández: Methodology; Investigation; Formal analysis. Alejandro Pedro Ayala: Methodology; Investigation; Formal analysis. Tayná Vitória Ramos de Oliveira: Writing – original draft; Methodology; Formal analysis. Ralph Santos-Oliveira: Writing – review & editing; Supervision; Investigation; Funding acquisition; Formal analysis; Data curation. Alan Silva de Menezes: Writing – original draft; Visualization; Resources; Investigation; Formal analysis. Beatriz da Silva Batista: Writing – original draft; Methodology; Formal analysis. Luciana Magalhães Rebelo Alencar: Visualization; Software; Resources; Investigation; Formal analysis; Conceptualization. Luelc de Souza Costa: Visualization; Software; Resources; Investigation; Formal analysis. Pierre Basílio Almeida Fechine: Writing – review & editing; Visualization; Supervision; Project administration; Funding acquisition; Conceptualization.

Supporting Information
The Supplementary Information contains the element distribution maps for the h-BN, h-BN-1P, and h-BN-1.5P samples obtained through EDS and the lower magnification TEM images of h-BN, h-BN-1P, and h-BN-1.5P.

Declaration of competing interest
The authors confirm that there are no personal or financial conflicts of interest that may have affected the outcomes or interpretation of this work.

Acknowledgments
The authors thank the Brazilian funding agencies for their support: CAPES (Finance Code 001-PROEX 23038.000509/2020–82), CNPq (PQ-Grant No. 313324/2021-2 and 308452/2022–4) and FAPEMA (Grants No. UNIVERSAL-06931/22, INFRA-02203/21, and ACT-02512/23). The authors also acknowledge the TEM facilities provided by the Brazilian Nanotechnology National Laboratory (LNNano/CNPEM).

Data availability
Data will be made available on request.

References

[1] Baig, N., Kammakakam, I., Falath, W. *et al.* Nanomaterials: A review of synthesis methods, properties, recent progress, and challenges. *Mater Adv* **2**, 1821–1871 (2021).

[2] Baig, N. Two-dimensional nanomaterials: A critical review of recent progress, properties, applications, and future directions. Compos Part A Appl Sci Manuf 165, 107362 (2023).

[3] Wang, L., Lou, Z. & Shen, G. 2020. 2D Nanomaterials with Hierarchical Architecture for Flexible Sensor Application. In: Singh and Mahapatra (eds.) 2D Nanomaterials for Advanced Applications, pp. 93–116. American Chemical Society, Washington, DC.

[4] Wen, X., Gong, Z. & Li, D. Nonlinear optics of two-dimensional transition metal dichalcogenides. *InfoMat.* **1**, 317–337 (2019).

[5] Bilal, M., Ullah Rashid, E., Zdarta, J. et al. Graphene-based nanoarchitectures as ideal supporting materials to develop multifunctional nanobiocatalytic systems for strengthening the biotechnology industry. Chemical Engineering Journal 452, 139509 (2023).

[6] Anghel, E., Simionescu, O.-G., Pachiu, C. *et al.* PREPARATION, RAMAN SPECTROSCOPY AND MORPHOLOGYCAL ANALYSIS OF VERTICALLY ALIGNED GRAPHENE NANOSHEETS. *U.P.B Sci. Bull., Series B* **82**, 181–190 (2020).

[7] Strojny-Cieślak, B., Pruchniewski, M., Sosnowska, M. et al. Toxicological insights into graphene family materials: Cytochrome P450 modulation and cellular stress in liver cells. Science of the Total Environment 974, 179211 (2025).

[8] Malavekar, D., Pawar, D., Bagde, A. et al. Advancements in graphene and its derivatives based composite Materials: A comprehensive review on Synthesis, Characterization, and supercapacitive charge storage. Chemical Engineering Journal 501, 157533 (2024).

[9] AlHumaidan, F.S., Vinoba, M., Ali, D. *et al.* Graphene derivatives formation from waste asphaltenes for use as electroactive materials in supercapacitors. *Results in Surfaces and Interfaces* **20**, 100569 (2025).

[10] Fu, X., Liu, Y., Wang, X. et al. Graphene-based advanced materials for energy storage and conversion systems: Progress, challenges, and commercial future. Appl Energy 386, 125566 (2025).

[11] Singh, A.K., Chaudhary, V., Singh, A.K. *et al.* Tuning of electronic properties of chemical vapor deposition grown graphene via self-assembled monolayer doping. *Mater Today Proc* **46**, 2919–2924 (2021).

[12] Rani, S. & Ray, S.J. 2020. Graphene and hexagonal boron nitride based nano-electronic biosensor. In: 2020 5th IEEE International Conference on Emerging Electronics, ICEE 2020. p. 1. Institute of Electrical and Electronics Engineers Inc.

[13] Lu, Y., Zhao, R., Wang, L. et al. Boron nitride nanotubes and nanosheets: Their basic properties, synthesis, and some of applications. Diam Relat Mater 136, 109978 (2023).

[14] Golberg, D., Bando, Y., Huang, Y. et al. Boron Nitride Nanotubes and Nanosheets. ACS Nano 4, 2979–2993 (2010).

[15] Weng, Q., Wang, X., Wang, X. et al. Functionalized hexagonal boron nitride nanomaterials: Emerging properties and applications. Chem Soc Rev 45, 3989–4012 (2016).

[16] Jedrzejczak-Silicka, M., Trukawka, M., Dudziak, M. et al. Hexagonal Boron Nitride Functionalized with Au Nanoparticles—Properties and Potential Biological Applications. Nanomaterials 8, 605 (2018).

[17] Ali, S., Ismail, P.M., Humayun, M. *et al.* Hexagonal boron nitride: From fundamentals to applications. *Desalination* **599**, 118442 (2025).

[18] Wen, W., Song, Y., Yan, X. *et al.* Recent advances in emerging 2D nanomaterials for biosensing and bioimaging applications. *Materials Today* **21**, 164–177 (2018).

[19] Bouziani, M., Bouziani, A., Zaari, H. et al. Tuning the optical and photocatalytic properties of hexagonal boron nitride through Fe

and co doping: A DFT study. Comput Theor Chem 1245, 115095 (2025).

[20] Kaya, O., Gabatel, L., Bellani, S. *et al.* 2D Hexagonal Boron Nitride-based Anticorrosion Coatings. *Materials Science* **8**, 042002 (2024).

[21] Verma, C., Dubey, S., Barsoum, I. *et al.* Hexagonal boron nitride as a cutting-edge 2D material for additive application in anticorrosive coatings: Recent progress, challenges and opportunities. *Mater Today Commun* **35**, 106367 (2023).

[22] Zahoor, M., Khan, S., Ismail, P.M. *et al.* 2024. Chapter 1 - Introduction to hexagonal boron nitrides: history, classification, structure, fundamental properties, challenges, and future perspective. In: Deshmukh, K., Pandey, M., and Mustansar Hussain, C. (eds.), *Hexagonal Boron Nitride*, pp. 3–28. Elsevier.

[23] Ali, S., Ullah, S., Ismail, P.M. *et al.* 2024. Chapter 21 - Molecular dynamic simulations and computational modeling of hexagonal boron nitride. In: Deshmukh, K., Pandey, M., and Mustansar Hussain, C. (eds.), *Hexagonal Boron Nitride*, pp. 589–610. Elsevier.

[24] Revabhai, P.M., Singhal, R.K., Basu, H. *et al.* Progress on boron nitride nanostructure materials: properties, synthesis and applications in hydrogen storage and analytical chemistry. *J Nanostructure Chem* **13**, 1–41 (2023).

[25] Zahoor, M., Ismail, P.M., Khan, S. *et al.* 2024. Hexagonal boron nitride for water desalination and wastewater treatment. In: Deshmukh, K., Pandey, M., Hussain, C. M. (eds), *Hexagonal Boron Nitride: Synthesis, Properties, and Applications,* pp. 457–482. Elsevier.

[26] Ali, S., Haneef, M., Akbar, J. *et al.* Single Au atom supported defect mediated boron nitride monolayer as an efficient catalyst for acetylene hydrochlorination: A first principles study. *Molecular Catalysis* **511**, 111753 (2021).

[27] Kamran, A.W., Zahoor, M., Ali, H. *et al.* Chromate ions chemisorption over the exterior surface of pristine boron nitride (B12N12) nanocage: A computational study. *Inorg Chem Commun* **148**, 110370 (2023).

[28] Dastgeer, G., Nisar, S., Zulfiqar, M.W. *et al.* A review on recent progress and challenges in high-efficiency perovskite solar cells. *Nano Energy* **132**, 110401 (2024).

[29] Dastgeer, G., Zulfiqar, M.W., Nisar, S. *et al.* Emerging Role of 2D Materials in Photovoltaics: Efficiency Enhancement and Future Perspectives. *Nanomicro Lett* **18**, 32 (2026).

[30] Panchanan, S., Dastgeer, G., Dutta, S. *et al.* Cerium-based halide perovskite derivatives: A promising alternative for lead-free narrowband UV photodetection. *Matter* **7**, 3949–3969 (2024).

[31] Nisar, S., Dastgeer, G., Zafar, M.S. *et al.* Optimizing Light Sensing Capabilities of WSe2 FETs through Chemical Modulation of Carrier Dynamics. *Opt Mater (Amst)* **158**, 116489 (2025).

[32] Dastgeer, G., Nisar, S., Rasheed, A. *et al.* Atomically engineered, high-speed non-volatile flash memory device exhibiting multibit data storage operations. *Nano Energy* **119**, 109106 (2024).

[33] Dastgeer, G., Shahzad, Z.M., Chae, H. *et al.* Bipolar Junction Transistor Exhibiting Excellent Output Characteristics with a Prompt Response against the Selective Protein. *Adv Funct Mater* **32**, 2204781 (2022).

[34] Zhang, J., Zhang, B., Yu, Y. *et al.* Regulating the electronic and optic properties of hexagonal boron nitride nanosheets via phosphorus doping. *EPL* **129**, 37001 (2020).

[35] Talukdar, D., Bora, S.S. & Ahmed, G.A. Electronic, optical, and adsorption properties of Li-doped hexagonal boron nitride: a GW approach. *Physical Chemistry Chemical Physics* **26**, 4021–4028 (2024).

[36] Yang, G., Chen, L., Liu, J. *et al.* Boron nitride nanosheets for biosensors and biomedicine. *TrAC - Trends in Analytical Chemistry* **191**, 118379 (2025).

[37] Lin, B., Xu, F., Mei, Y. *et al.* Phosphorus-doped h-boron nitride as an efficient metal-free catalyst for direct dehydrogenation of ethylbenzene. *Catal Sci Technol* **11**, 5590–5597 (2021).

[38] Li, Y., Li, H., Li, R. *et al.* Preparation of phosphorus-doped boron nitride and its adsorption of heavy metals from flue gas. *R Soc Open Sci* **7**, 200079 (2020).

[39] Yu, L.-F., Xu, J.-Y., Shen, C. *et al.* Realizing ultra-low thermal conductivity by strong synergy of asymmetric geometry and electronic structure in boron nitride and arsenide. *Rare Metals* **42**, 210–221 (2022).

[40] Mukhopadhyay, T.K., Ghosh, A. & Datta, A. Screening 2D Materials for Their Nanotoxicity toward Nucleic Acids and Proteins: An In Silico Outlook. *ACS Physical Chemistry Au* **4**, 97–121 (2024).

[41] Santos, J., Moschetta, M., Rodrigues, J. *et al.* Interactions Between 2D Materials and Living Matter: A Review on Graphene and Hexagonal Boron Nitride Coatings. *Front Bioeng Biotechnol* **9**, 612669 (2021).

[42] Merlo, A., Mokkapati, V.R.S.S., Pandit, S. *et al.* Boron nitride nanomaterials: biocompatibility and bio-applications. *Biomater Sci* **6**, 2298–2311 (2018).

[43] Czarniewska, E., Mrówczyńska, L., Jędrzejczak-Silicka, M. *et al.* Non-cytotoxic hydroxyl-functionalized exfoliated boron nitride nanoflakes impair the immunological function of insect haemocytes in vivo. *Sci Rep* **9**, 14027 (2019).

[44] Mateti, S., Wong, C.S., Liu, Z. *et al.* Biocompatibility of boron nitride nanosheets. *Nano Res* **11**, 334–342 (2018).

[45] Mirzaee, M., Rashidi, A., Zolriasatein, A. *et al.* A simple, low cost, and template-free method for synthesis of boron nitride using different precursors. *Ceram Int* **47**, 5977–5984 (2021).

[46] Li, S., Lu, X., Lou, Y. *et al.* The Synthesis and Characterization of h-BN Nanosheets with High Yield and Crystallinity. *ACS Omega* **6**, 27814–27822 (2021).

[47] Itskou, I., Kafizas, A., Nevjestic, I. *et al.* Effects of Phosphorus Doping on Amorphous Boron Nitride's Chemical, Sorptive, Optoelectronic, and Photocatalytic Properties. *Journal of Physical Chemistry C* **128**, 13249–13263 (2024).

[48] Abat, M., Degryse, F., Baird, R. *et al.* Formulation, synthesis and characterization of boron phosphate (BPO4) compounds as raw materials to develop slow-release boron fertilizers. *Journal of Plant Nutrition and Soil Science* **177**, 860–868 (2014).

[49] Riyas, Z.M., Sharmila, S., Priya, P. *et al.* Nanoengineering of hexagonal boron nitride (h-BN) decorated on La2O3 nanocomposite as an efficient electrode material for asymmetric supercapacitor application. *Ionics (Kiel)* **31**, 4991–5011 (2025).

[50] Gurbuz, H.N., Yilmaz, K., Ipekci, H.H. *et al.* Synthesis and characterization of new targeted pH-responsive heteroatom-doped hexagonal boron nitride nanosheets for controlled drug release. *Materials Science and Engineering: B* **299**, 116909 (2024).

[51] Zheng, M., Gu, Y., Xu, Z. *et al.* Synthesis and characterization of boron nitride nanoropes. *Mater Lett* **61**, 1943–1945 (2007).

[52] Gouin, X., Grange, P., Bois, L. *et al.* Characterization of the nitridation process of boric acid. *J Alloys Compd* **224**, 22–28 (1995).

[53] Basu, N., Bharathi, M.S.S., Sharma, M. *et al.* Large Area Few-Layer Hexagonal Boron Nitride as a Raman Enhancement Material. *Nanomaterials* **11**, 622 (2021).

[54] Lee, S.H., Jeong, H., Okello, O.F.N. *et al.* Improvements in structural and optical properties of wafer-scale hexagonal boron nitride film by post-growth annealing. *Sci Rep* **9**, 10590 (2019).

[55] Seo, J.W., Pophali, A., An, S. *et al.* Fundamental structural study of hexagonal boron nitride (h-BN) and boron nitride nanotube (BNNT) at low and high temperatures. *J Mol Struct* **1319**, 139545 (2025).

[56] Haque, A. & Narayan, J. Conversion of h-BN into c-BN for tuning optoelectronic properties. *Mater Adv* **1**, 830–836 (2020).

[57] Acharya, L., Babu, P., Behera, A. *et al.* Novel synthesis of boron nitride nanosheets from hexagonal boron nitride by modified aqueous phase bi-thermal exfoliation method. *Mater Today Proc* **35**, 239–242 (2021).

[58] Spiridonov, D.M., Henaish, A.M.A., Vokhmintsev, A.S. *et al.* Diffuse reflectance spectral features of hexagonal boron nitride nanopowder. *AIP Conf Proc* **1886**, 020021 (2017).

[59] Li, Q., Gao, T., Zhang, K. *et al.* Tuning Electronic Structure and Optical Properties of Monolayered h-BN by Doping C, Cu and Al. *Molecules* **30**, 192 (2025).

[60] Zunger, A., Katzir, A. & Halperin, A. Optical properties of hexagonal boron nitride. *Phys Rev B* **13**, 5560–5573 (1976).

[61] Medeiros, S.E.L. & Azevedo, S. Electronic and optical properties of quantum emitters in h-BN. *Appl Phys A Mater Sci Process* **129**, 659 (2023).

[62] Román, R.J.P., Costa, F.J.R., Zobelli, A. *et al.* Band gap measurements of monolayer h-BN and insights into carbon-related point defects. *2d Mater* **8**, 044001 (2021)

[63] Zhu, Y.C., Bando, Y., Xue, D.F. *et al.* New boron nitride whiskers: Showing strong ultraviolet and visible light luminescence. *Journal of Physical Chemistry B* **108**, 6193–6196 (2004).

[64] Rand, M.J. & Roberts, J.F. Preparation and Properties of Thin Film Boron Nitride. *J Electrochem Soc* **115**, 423–429 (1968).

[65] Ba, K., Jiang, W., Cheng, J. *et al.* Chemical and Bandgap Engineering in Monolayer Hexagonal Boron Nitride. *Sci Rep* **7**, 45584 (2017).

[66] Ding, Y., Zeng, M., Zheng, Q. *et al.* Bidirectional and reversible tuning of the interlayer spacing of two-dimensional materials. *Nat Commun* **12**, 5886 (2021).

[67] Zhen, Z.Q., Cui, H.L. & Wang, H.Y. Study of the electronic, elastic, piezoelectric and infrared properties of trigonal BPO4. *Mater Today Commun* **36**, (2023).

[68] Ma, X., Shi, Z., Zang, H. *et al.* Efficient n-Type Doping of Hexagonal Boron Nitride via Localized Band-Offset Compensation Strategy. *Small* 2501962 (2025).

[69] Fukamachi, S., Solís-Fernández, P., Kawahara, K. *et al.* Large-area synthesis and transfer of multilayer hexagonal boron nitride for enhanced graphene device arrays. *Nat Electron* **6**, 126–136 (2023).

[70] Wu, X., Ge, R., Chen, P.-A. *et al.* Thinnest Nonvolatile Memory Based on Monolayer h-BN. *Advanced Materials* **31**, 1806790 (2019).

[71] Yang, X., Liu, P., Zhou, D. *et al.* High temperature performance of coaxial h -BN/CNT wires above 1,000 °C: Thermionic electron emission and thermally activated conductivity. *Nano Res.*1855–1861 (2019).

[72] Dweydari, A.W. & Mee, C.H.B. Work function measurements on (100) and (110) surfaces of silver. *physica status solidi (a)* **27**, 223–230 (1975).

[73] Chatterjee, S., Luo, Z., Acerce, M. *et al.* Chemical Vapor Deposition of Boron Nitride Nanosheets on Metallic Substrates via Decaborane/Ammonia Reactions. *Chemistry of Materials* **23**, 4414–4416 (2011).

[74] Yang, X., Zhang, R., Pu, J. *et al.* 2D graphene and h-BN layers application in protective coatings. *Corrosion Reviews* **39**, 93–107 (2021).

[75] Sohn, A., Moon, H., Kim, J. *et al.* Band Alignment at Au/MoS2 Contacts: Thickness Dependence of Exfoliated Flakes. *Journal of Physical Chemistry C* **121**, 22517–22522 (2017).

[76] Kim, H. & Choi, H.J. Thickness dependence of work function, ionization energy, and electron affinity of Mo and W dichalcogenides from DFT and GW calculations. *Phys Rev B* **103**, 085404 (2021).

[77] Luo, W., Yang, T., Su, L. *et al.* Preparation of hexagonal BN whiskers synthesized at low temperature and their application in fabricating an electrochemical nitrite sensor. *RSC Adv* **6**, 27767–27774 (2016).

[78] Chen, L., Huang, M., Luo, T. *et al.* A low-temperature route to nanocrystalline boron nitride whiskers and flakes. *Mater Lett* **58**, 3634–3636 (2004).

[79] Niu, H.-T., Xiao, G., He, X.-H. *et al.* Preparation of quasi-isotropic thermal conductive composites by interconnecting spherical alumina and 2D boron nitride flakes. *Rare Metals* **42**, 1283–1293 (2023).

[80] Hod, O. Graphite and hexagonal boron-nitride have the same interlayer distance. Why? *J Chem Theory Comput* **8**, 1360–1369 (2012).

[81] Su, C., Janzen, E., He, M. *et al.* Fundamentals and emerging optical applications of hexagonal boron nitride: a tutorial. *Adv Opt Photonics* **16**, 229–343 (2024).

[82] Liang, J., Huang, Y., Lin, J. *et al.* In-situ conversion of porous boron nitride to highly crystallized nanoplates-assembled hexagonal boron nitride nanoarchitectures via a metal ion-assisted annealing method. *J Alloys Compd* **705**, 749–755 (2017).

[83] Alkoy, S., Toy, C., Gdniil, T. *et al.* Crystallization Behavior and Characterization of Turbostratic Boron Nitride. *J Eur Ceram Soc* **17**, 1415–1422 (1997).

[84] Kumar, A., Malik, G., Sharma, S. *et al.* Precursors controlled morphologies of nanocrystalline h-BN and its growth mechanism. *Ceram Int* **47**, 30985–30992 (2021).

[85] Zhang, J., Neupane, N., Dahal, P.R. *et al.* Antibiotic-Loaded Boron Nitride Nanoconjugate with Strong Performance against Planktonic Bacteria and Biofilms. *ACS Appl Bio Mater* **6**, 3131–3142 (2023).

[86] Hilder, T.A. & Gaston, N. Interaction of Boron Nitride Nanosheets with Model Cell Membranes. *ChemPhysChem* **17**, 1573–1578 (2016).

[87] Wu, P., Song, X., Lu, L. *et al.* Understanding oxygen doping effects on boron nitride catalysis for efficient oxidative desulfurization of fuel oil. *Appl Catal B* **347**, 123784 (2024).

[88] Li, H., Zhu, S., Zhang, M. *et al.* Tuning the Chemical Hardness of Boron Nitride Nanosheets by Doping Carbon for Enhanced Adsorption Capacity. *ACS Omega* **2**, 5385–5394 (2017).

[89] Gutru, R., Turtayeva, Z., Xu, F. *et al.* Recent progress in heteroatom doped carbon based electrocatalysts for oxygen reduction reaction in anion exchange membrane fuel cells. *Int J Hydrogen Energy* **48**, 3593–3631 (2023).

[90] Yu, W., Wang, K., Li, H. *et al.* An updated review of few-layer black phosphorus serving as a promising photocatalyst: synthesis, modification and applications. *Nanoscale* **16**, 19131–19173 (2024).

[91] Sharmin, N., Hasan, M.S., Parsons, A.J. *et al.* Effect of Boron Addition on the Thermal, Degradation, and Cytocompatibility Properties of Phosphate-Based Glasses. *Biomed Res Int* **2013**, 902427 (2013).

[92] Yu, Y., Lu, L., Yang, Q. *et al.* Using MoS2Nanomaterials to Generate or Remove Reactive Oxygen Species: A Review. *ACS Appl Nano Mater* **4**, 7523–7537 (2021).

[93] Wang, C., Long, Y., Deng, Y. *et al.* Hexagonal boron nitride nanomaterials for biomedical applications. *BMEMat* **2**, e12068 (2024).

[94] Cai, Y., Zhang, G. & Zhang, Y.-W. Electronic Properties of Phosphorene/Graphene and Phosphorene/Hexagonal Boron nitride Heterostructures. *Journal of Physical Chemistry C* **119**, 13929–13936 (2015).

[95] Lin, M., Qi, W., Zhang, H. *et al.* Boron doped nanomaterials for photocatalysis. *Journal of Photochemistry and Photobiology C: Photochemistry Reviews* **60–61**, 100679 (2024).

[96] Pillai, V. V., Ramasubramanian, B., Sequerth, O. *et al.* Nanomaterial advanced smart coatings: Emerging trends shaping the future. *Appl Mater Today* **42**, 102574 (2025).

[97] Duo, Y., Xie, Z., Wang, L. *et al.* Borophene-based biomedical applications: Status and future challenges. *Coord Chem Rev* **427**, 213549 (2021).

[98] Andrade-Alarcón, D., de la Asunción-Nadal, V., Crespo, G.A. *et al.* Tailored Core-Shell Nanocarrier for Therapeutic Drug Delivery via Visible Light Activation. *Angewandte Chemie - International Edition* e202514317 (2025).

[99] Sasikumar, G.K., Anitha, A., Sivanandam, M. *et al.* Phosphorus doped 2D polymeric graphitic carbon nitride biomaterial: Biological activity and DFT insights with nitrofuran drug interactions. *Mater Sci Semicond Process* **202**, 110117 (2026).

[100] Kwak, M.S., Park, Y.-J., Kim, M.P. *et al.* Interfacial Polarization for High-Performance Triboelectric Devices: Principles, Strategies, and Applications. *ACS Appl Mater Interfaces* **17**, 37336–37352 (2025).

[101] Teixeira do Nascimento, A., Stoddart, P.R., Goris, T. *et al.* Stimuli-Responsive Materials for Biomedical Applications. *Advanced Materials* **37**, e07559 (2025).